

Supporting Information

Leveraging Coordination Chemistry in the Design of Bipolar Energy Storage Materials for Redox Flow Batteries

Mathias L. Skavenborg,^{a,b} James N. McPherson,^a Alexandros Pasadakis-Kavounis,^c Johan Hjelm,^c T. David Waite,^b Christine J. McKenzie^a

^a Department of Physics, Chemistry and Pharmacy, University of Southern Denmark, 5230 Odense M, Denmark.

^b Water Research Centre, School of Civil and Environmental Engineering, University of New South Wales, Sydney, New South Wales, Australia.

^c Technical University of Denmark Department of Energy Conversion and Storage, Fysikvej, Building 310, 2800 Kgs Lyngby, Denmark

Single Crystal X-Ray Diffraction Structure Refinements

Hpsq (CCDC 2125216)

Colourless plates of **Hpsq** grew from the slow evaporation of solvent from a concentrated solution of **Hpsq** in acetone/water (1:1 v/v). The coordinates of the hydrogen atom H2 which is bound to the sulfonamide nitrogen, N2, were freely refined but its isotropic thermal parameter was fixed at 150% of the equivalent displacement parameter of the heavy N2 atom.

[Zn(**psq**)₂].0.4(MeCN) (CCDC 2125217)

Colourless rods of [Zn(**psq**)₂].0.4(MeCN) grew as solvent evaporated from a concentrated solution of [Zn(**psq**)₂] in MeCN. Additional non-merohedral twin components were observed in the diffraction pattern, however the most satisfactory statistics were obtained when the (weak) reflections due to these small twin components were ignored. The structure was solved and refined in the non-centrosymmetric *P* 2₁2₁2₁ space group, with a small (9%) racemic twin component. Solvent accessible voids within the structure are partially occupied by acetonitrile. The occupancy of the acetonitrile molecule (40%) was refined freely, while the anisotropic displacement parameters for the carbon and nitrogen atoms in the acetonitrile molecule were restrained to a rigid body model using the RIGU command.

[Co(**psq**)₂] (CCDC 2125219)

Orange blocks of [Co(**psq**)₂] grew as diethyl ether slowly diffused into a concentrated solution of [Co(**psq**)₂] in acetonitrile. An additional non-merohedral twin component was observed in the diffraction pattern, however the most satisfactory model and statistics were obtained when the (weak) reflections due to the small twin component (~14%) were ignored. The structure was solved and refined in the non-centrosymmetric *P* 2₁ spacegroup. One of the **psq**⁻ ligands was disordered over two positions (with occupancies freely refined to 60% and 40%). Carbon and nitrogen atoms (except the sulfonamido nitrogen atom N5/N7) in the disordered **psq**⁻ which positionally overlapped with another atom of the same type were modelled as a single atom with 100% occupancy, rather than being split into the two components, to improve the data : parameter ratio. RIGU and SIMU commands were used to keep the anisotropic displacement parameters for the atoms in the disordered **psq**⁻ ligand (the overlapping atoms C21/S3, C32/S2 and N5/N7 in particular) stable during refinement. Each of the three bonds involving the sulfonamido nitrogen atoms (Co-N, N-S and N-C_{ipso}) were restrained to be the same as the corresponding bonds across all three sulfonamido groups (N2, N5 and N7).

[Co(**psq**)₂][PF₆](MeCN) (CCDC 2125218)

Dark brown lathes of [Co(**psq**)₂][PF₆](MeCN) grew from a green solution of [Co(**psq**)₂] and (NH₄)₂[Ce(NO₃)₆] (3 equiv.) in acetonitrile/water (5.5 mL, 10:1, v/v) which was left to stand overnight. One of the **psq**⁻ ligands was disordered across two sites (~3:1). Some of the C atoms in the minor component of this disorder were not stable to refinement with anisotropic displacement parameters, despite the use of RIGU and SIMU restraints, and so instead were modelled with freely refined isotropic thermal parameters. The N and C atoms of the quinoline group in the minor component of the **psq**⁻ ligand disorder (N7 and C29...C37) were modelled as an ideal naphyl ring. Corresponding 1,2- and 1,3- atomic separations within each of the three **psq**⁻ residues were restrained to similar values using the SAME command. A molecule of acetonitrile solvent was also located in the lattice, which was also disordered over two positions (~3:1). The [PF₆]⁻ anion was modelled across three positions (1/3 occupancy each), with all P-F bond lengths restrained to the same free variable, while all the *cisoid* F...F 1,3-separations restrained to 141.4% of the P-F bond lengths, using DFIX and DANG commands, respectively. The pair of opposite fluorine atoms F3B and F4B were constrained to have the same anisotropic displacement parameters using an EADP command.

Crystallographic Data

Table S1. Crystal data and details of X-ray diffraction data collections

Name:	Hpsq	[Zn(ψsq) ₂]-0.4(MeCN)	[Co(ψsq) ₂]	[Co(ψsq) ₂][PF ₆](MeCN)
CCDC Identifier:	2125216	2125217	2125219	2125218
Empirical formula	C ₁₄ H ₁₁ N ₃ O ₂ S	C _{28.81} H _{21.21} N _{6.4} O ₄ S ₂ Zn	C ₂₈ H ₂₀ CoN ₆ O ₄ S ₂	C ₃₀ H ₂₃ N ₇ O ₄ F ₆ PS ₂ Co
Formula weight	285.32	650.55	627.55	813.57
Temperature/K	100.01(10)	100.00(10)	100.01(10)	100.01(10)
Crystal system	triclinic	orthorhombic	monoclinic	monoclinic
Space group	P-1	P2 ₁ 2 ₁ 2 ₁	P2 ₁	P2 ₁ /n
a/Å	7.7548(2)	8.8155(2)	9.0826(5)	11.63680(10)
b/Å	9.2240(2)	13.9211(3)	9.4773(3)	8.69800(10)
c/Å	9.5012(3)	23.9805(5)	15.0534(7)	31.4543(3)
α/°	94.487(2)	90	90	90
β/°	111.101(2)	90	96.842(5)	97.3370(10)
γ/°	91.556(2)	90	90	90
Volume/Å ³	630.99(3)	2942.92(11)	1286.55(10)	3157.64(5)
Z	2	4	2	4
ρ _{calc} /cm ³	1.502	1.468	1.620	1.711
μ/mm ⁻¹	2.334	2.876	7.170	6.758
F(000)	296.0	1331.0	642.0	1648.0
Crystal size/mm ³	0.088 × 0.036 × 0.013	0.156 × 0.028 × 0.013	0.123 × 0.062 × 0.052	0.426 × 0.046 × 0.025
Radiation	Cu Kα (λ = 1.54184)	Cu Kα (λ = 1.54184)	Cu Kα (λ = 1.54184)	Cu Kα (λ = 1.54184)
2θ range for data collection/°	9.636 to 149.356	7.342 to 149.374	5.914 to 150.022	5.666 to 149.29
Index ranges	-9 ≤ h ≤ 9, -11 ≤ k ≤ 10, -11 ≤ l ≤ 11	-10 ≤ h ≤ 10, -16 ≤ k ≤ 17, -29 ≤ l ≤ 21	-11 ≤ h ≤ 10, -11 ≤ k ≤ 11, -18 ≤ l ≤ 18	-14 ≤ h ≤ 14, -10 ≤ k ≤ 10, -38 ≤ l ≤ 39
Reflections collected	18486	32902	36027	87217
Independent reflections	2515 [R _{int} = 0.0312, R _{sigma} = 0.0186]	5954 [R _{int} = 0.0513, R _{sigma} = 0.0349]	5125 [R _{int} = 0.0691, R _{sigma} = 0.0394]	6425 [R _{int} = 0.0285, R _{sigma} = 0.0114]
Data/restraints/parameters	2515/0/184	5954/9/400	5125/514/419	6425/1055/684
Goodness-of-fit on F ²	1.067	1.124	1.085	1.064
Final R indexes [I ≥ 2σ(I)]	R ₁ = 0.0287, wR ₂ = 0.0711	R ₁ = 0.0397, wR ₂ = 0.0881	R ₁ = 0.0678, wR ₂ = 0.1504	R ₁ = 0.0310, wR ₂ = 0.0745
Final R indexes [all data]	R ₁ = 0.0344, wR ₂ = 0.0738	R ₁ = 0.0428, wR ₂ = 0.0896	R ₁ = 0.0715, wR ₂ = 0.1528	R ₁ = 0.0326, wR ₂ = 0.0756
Largest diff. peak/hole / e Å ⁻³	0.30/-0.38	0.44/-0.36	0.72/-1.08	0.52/-0.35
Flack parameter		0.09(3)	-0.009(4)	

Numbering scheme

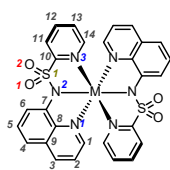


Table S2. Selected bond distances measured for Co(ps_q)₂, [Co(ps_q)₂][PF₆] and Zn(ps_q)₂

[Co(ps _q) ₂]		[Co(ps _q) ₂][PF ₆](MeCN)		[Zn(ps _q) ₂](0.4MeCN)	
atom	D / Å	atom	D / Å	atom	D / Å
Co1-N1	2.141(7)	Co1-N1	1.944(1)	Zn-N1	2.129(4)
Co1-N2	2.066(6)	Co1-N2	1.904(2)	Zn-N2	2.104(4)
Co1-N3	2.156(7)	Co1-N3	1.954(1)	Zn-N3	2.164(4)
Co1-N4	2.146(7)	Co1-N4	1.980(9)/ 2.027(9)	Zn-N4	2.254(4)
Co1-N5	2.08(2) 2.06(3)	Co1-N5A	1.906(6)/ 1.92(2)	Zn-N5	2.110(4)
Co1-N6	2.129(5)	Co1-N6	1.943(4)/ 1.85(3)	Zn-N6	2.214(4)

Table S3. Cis bond angles measured for Co(ps_q)₂, [Co(ps_q)₂][PF₆] and Zn(ps_q)₂.

[Co(ps _q) ₂]		[Co(ps _q) ₂][PF ₆](MeCN)		[Zn(ps _q) ₂](0.4MeCN)	
atom	θ / °	atom	θ / °	atom	θ / °
N1-Co1-N2	78.1(3)	N1-Co1-N2	83.23(6)	N1-Zn-N2	80.2(1)
N1-Co1-N4	90.7(3)	N1-Co1-N4	89.8(3) 93.8(3)	N1-Zn-N4	85.90(1)
N1-Co1-N5	98.7(7) 98(1)	N1-Co1-N5	93.5(2) 96.3(6)	N1-Zn-N5	106.4(2)
N1-Co1-N6	91.2(2)	N1-Co1-N6	92.7(1) 89(1)	N1-Zn-N6	93.4(1)
N2-Co1-N3	81.2(3)	N2-Co1-N3	86.51(7)	N2-Zn-N3	78.2(2)
N2-Co1-N4	97.4(3)	N2-Co1-N4	93.7(3) 92.2(3)	N2-Zn-N4	106.3(1)
N2-Co1-N6	102.0(2)	N2-Co1-N6	97.2(7) 97(1)	N2-Zn-N6	97.8(1)
N3-Co1-N4	94.4(3)	N3-Co1-N4	89.8(3) 87.6(3)	N3-Zn-N4	90.2(1)
N3-Co1-N5	102.1(7) 103(3)	N3-Co1-N5A	96.6(2) 94.0(6)	N3-Zn-N5	96.1(1)
N3-Co1-N6	90.7(2)	N3-Co1-N6	89.6(1) 92(1)	N3-Zn-N6	99.8(1)
N4-Co1-N5	76.3(7) 84(1)	N4-Co1-N5A	83.2(4) 83.0(7)	N4-Zn-N5	79.4(1)
N5-Co1-N6	84.1(7) 76(1)	N5A-Co1-N6	86.0(2) 88(1)	N5-Zn-N6	77.2(2)

Table S4. Trans bond angles measured for $\text{Co}(\text{psq})_2$, $[\text{Co}(\text{psq})_2]\text{PF}_6$ and $\text{Zn}(\text{psq})_2$.

$[\text{Co}(\text{psq})_2]$		$[\text{Co}(\text{psq})_2][\text{PF}_6] \cdot (\text{MeCN})$		$[\text{Zn}(\text{psq})_2] \cdot 0.4(\text{MeCN})$	
atom	$\theta / ^\circ$	atom	$\theta / ^\circ$	atom	$\theta / ^\circ$
N1-Co1-N3	159.2(3)	N1-Co1-N3	169.69(7)	N1-Zn-N3	156.0(1)
N4-Co1-N6	160.4(2)	N4-Co1-N6 N7-Co1-N9	169.1(3) 171(1)	N4-Zn-N6	155.4(1)
N2-Co1-N5/7	173.0(7) 175(1)	N2-Co1-N5/8	175.5(2) 175.1(6)	N2-Zn-N5	171.8(2)

^1H - and ^{13}C -NMR spectra of $\text{Co}(\text{psq})_2$, $[\text{Co}(\text{psq})_2]\text{PF}_6$ and $\text{Zn}(\text{psq})_2$

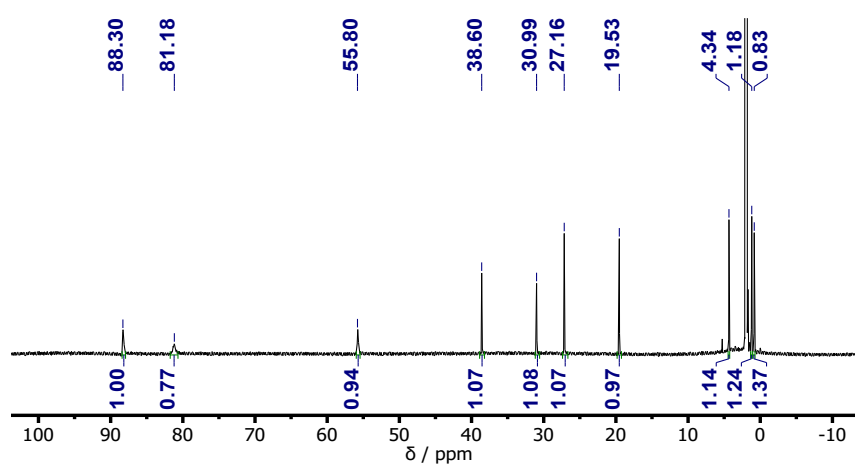


Figure S1. ^1H -NMR spectrum (400 MHz, CD_3CN) of $\text{Co}(\text{psq})_2$ from 100 ppm to -10 ppm.

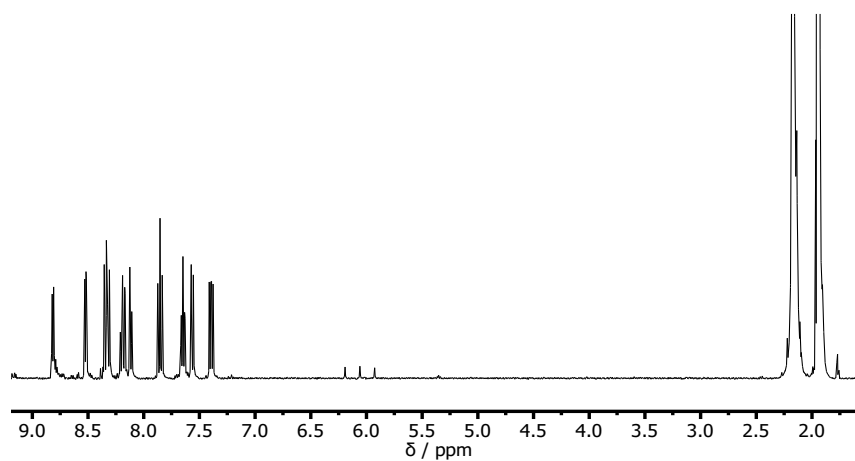


Figure S2. ^1H -NMR spectrum (400 MHz, CD_3CN) of $[\text{Co}(\text{psq})_2]\text{PF}_6$ from 9 ppm to 1 ppm.

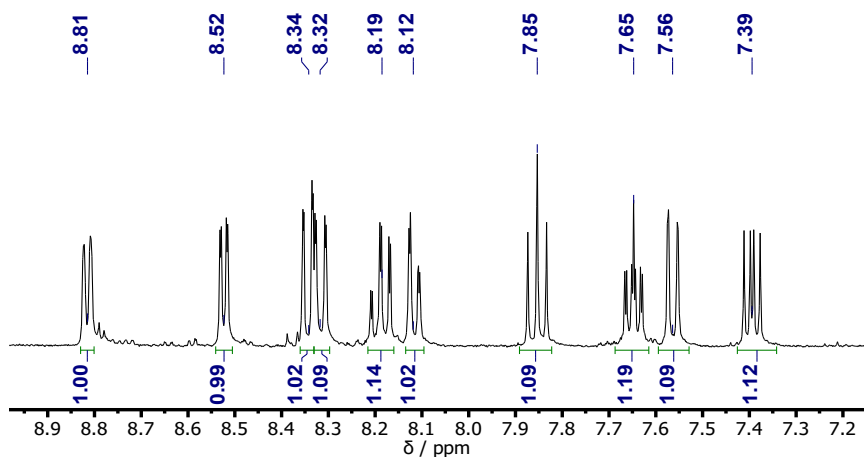


Figure S3. ^1H -NMR spectrum (400 MHz, CD_3CN) of $[\text{Co}(\text{psq})_2]\text{PF}_6$ from 9 ppm to 7 ppm.

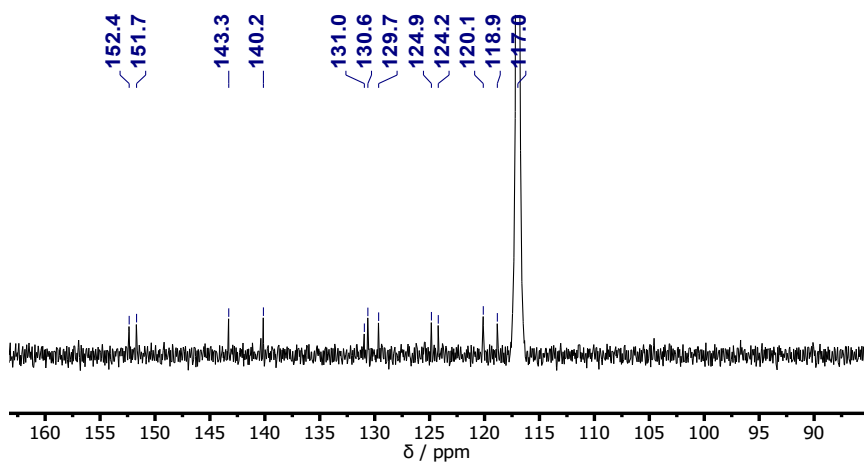


Figure S4. ^{13}C -NMR spectrum (100 MHz, CD_3CN) of $[\text{Co}(\text{psq})_2]\text{PF}_6$ from 165 ppm to 80 ppm.

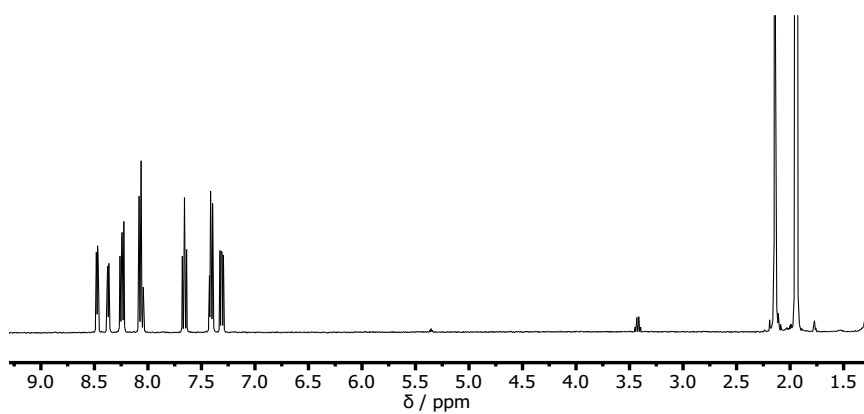


Figure S5. ^1H -NMR spectrum (400 MHz, CD_3CN) of $\text{Zn}(\text{psq})_2$ from 9.5 ppm to 1 ppm.

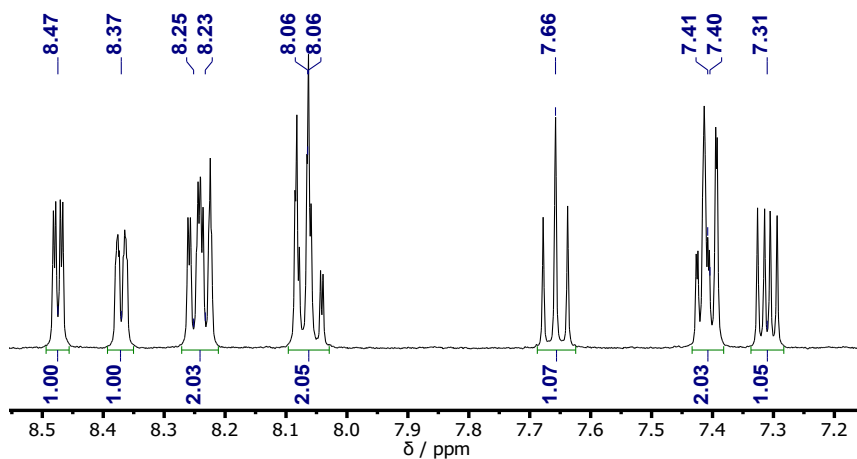


Figure S6. ^1H -NMR spectrum (400 MHz, CD_3CN) of $\text{Zn}(\text{psq})_2$ from 9 ppm to 7 ppm.

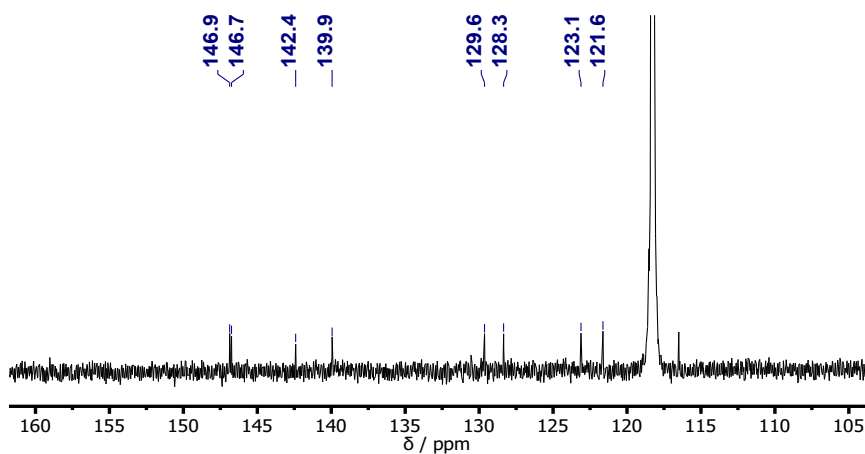


Figure S7. ^{13}C -NMR spectrum (100 MHz, CD_3CN) of $\text{Zn}(\text{psq})_2$ from 165 ppm to 105 ppm.

^1H DOSY NMR plots of $[\text{Co}(\text{psq})_2]\text{PF}_6$ and $\text{Zn}(\text{psq})_2$:

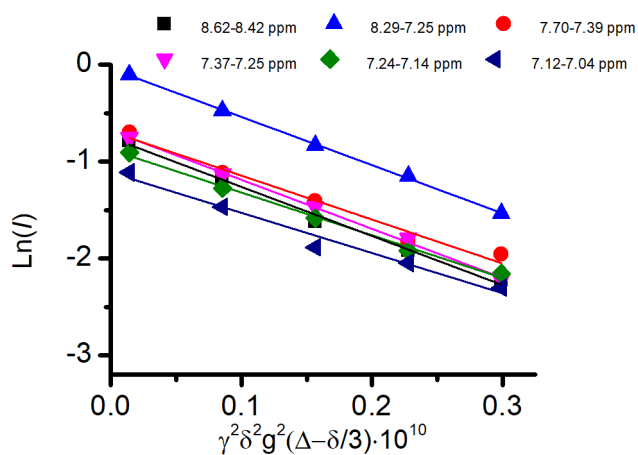
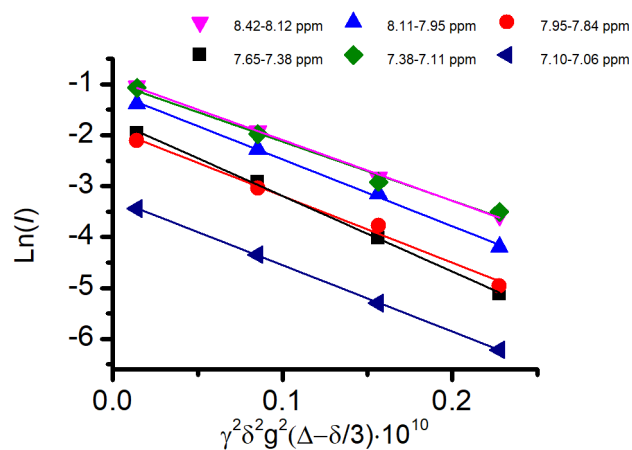


Figure S8. $[\text{Co}(\text{psq})_2]\text{PF}_6$ ^1H DOSY NMR data.

Table S5. [Co(psq)₂]PF₆ ¹H DOSY NMR data.

Integral / ppm	Fit	R ²	D ₀ ^a / 10 ⁻¹⁰ ·m ² /s	a ^b / Å
8.62-8.42	-5.07·10 ⁻¹⁰ - 0.75	0.990	5.07	9.6
8.29-7.25	-4.98·10 ⁻¹⁰ - 0.040	0.998	4.98	9.7
7.70-7.39	-4.54·10 ⁻¹⁰ - 0.69	0.972	4.54	10.7
7.37-7.25	-5.06·10 ⁻¹⁰ - 0.68	0.997	5.06	9.6
7.24-7.14	-4.14·10 ⁻¹⁰ - 0.88	0.997	4.14	11.7
7.12-7.04	-4.15·10 ⁻¹⁰ - 1.11	0.968	4.15	11.7

**Figure S9.** Zn(psq)₂ ¹H DOSY NMR data.**Table S6.** Zn(psq)₂ ¹H DOSY NMR data.

Integral / ppm	Fit	R ²	D ₀ ^a / 10 ⁻⁹ ·m ² /s	a ^b / Å
8.42-8.12	-1.20·10 ⁻⁹ - 6.01	0.997	1.20	4.0
8.11-7.95	-5.74·10 ⁻⁹ - 5.74	0.999	5.74	0.85
7.95-7.84	-1.31·10 ⁻⁹ - 5.02	0.987	1.31	3.7
7.65-7.38	-1.49·10 ⁻⁹ - 5.20	0.998	1.49	3.0
7.38-7.11	-1.60·10 ⁻⁹ - 5.94	0.985	1.60	3.0
7.10-7.06	-1.30·10 ⁻⁹ - 1.30	0.999	1.30	3.7

Electronic Spectra of $\text{Co}(\text{psq})_2$ and $[\text{Co}(\text{psq})_2]\text{PF}_6$

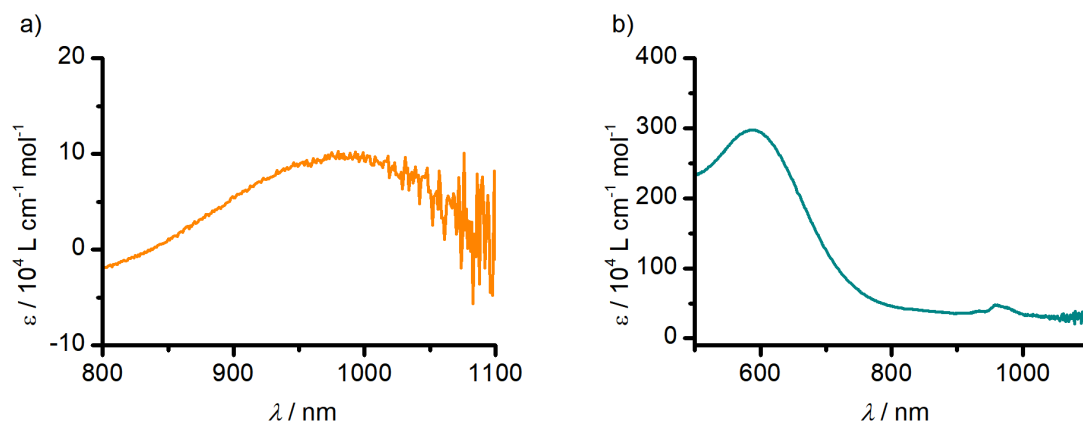


Figure S10. Electronic spectra of a) $\text{Co}(\text{psq})_2$ (0.734 mM) and b) $[\text{Co}(\text{psq})_2]\text{PF}_6$ (0.414 mM).

FTIR Spectra

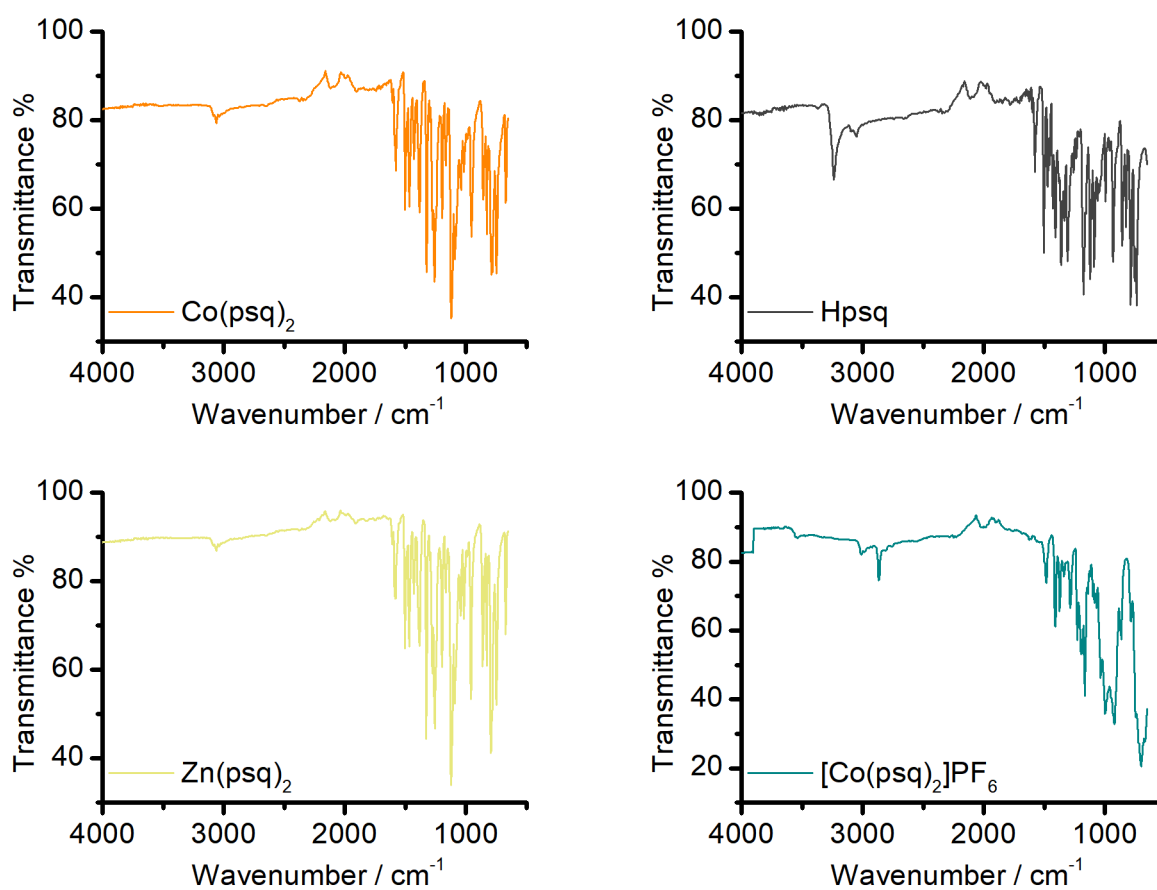


Figure S11. FTIR of $\text{Co}(\text{psq})_2$, $\text{Zn}(\text{psq})_2$, Hpsq and $[\text{Co}(\text{psq})_2]\text{PF}_6$.

Mass spectra of $\text{Co}(\text{psq})_2$, $[\text{Co}(\text{psq})_2]\text{PF}_6$ and $\text{Zn}(\text{psq})_2$

$\text{Co}(\text{psq})_2$

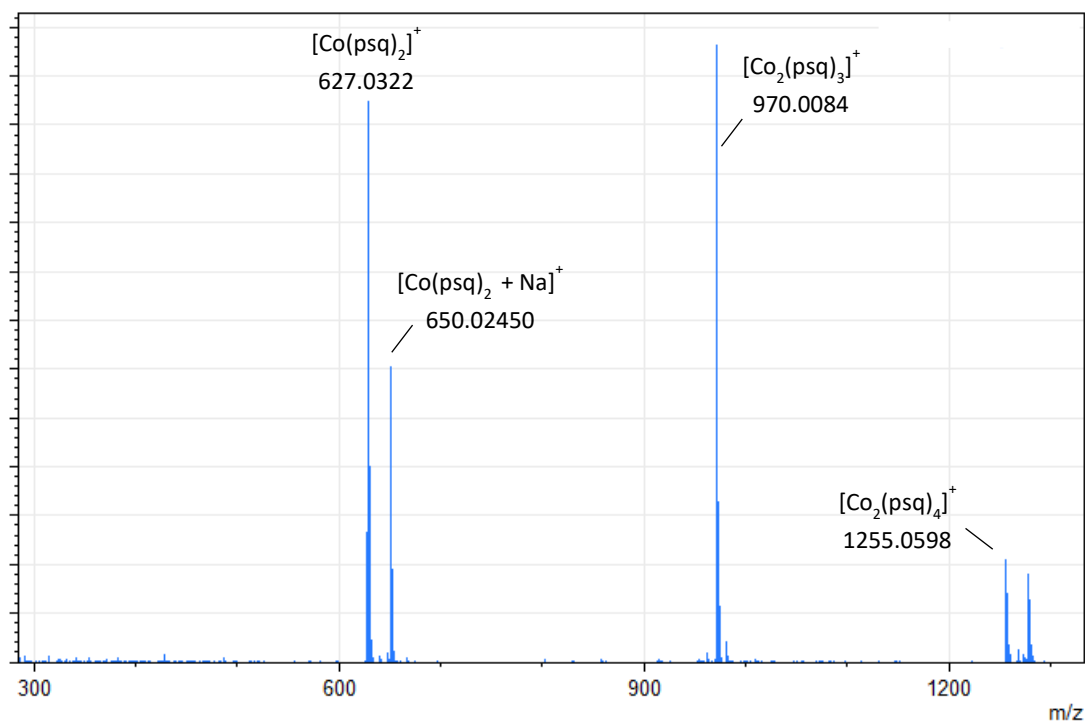


Figure S12. Mass spectrum (ESI, positive mode, MeCN) of $\text{Co}(\text{psq})_2$

$[\text{Co}(\text{psq})_2]\text{PF}_6$

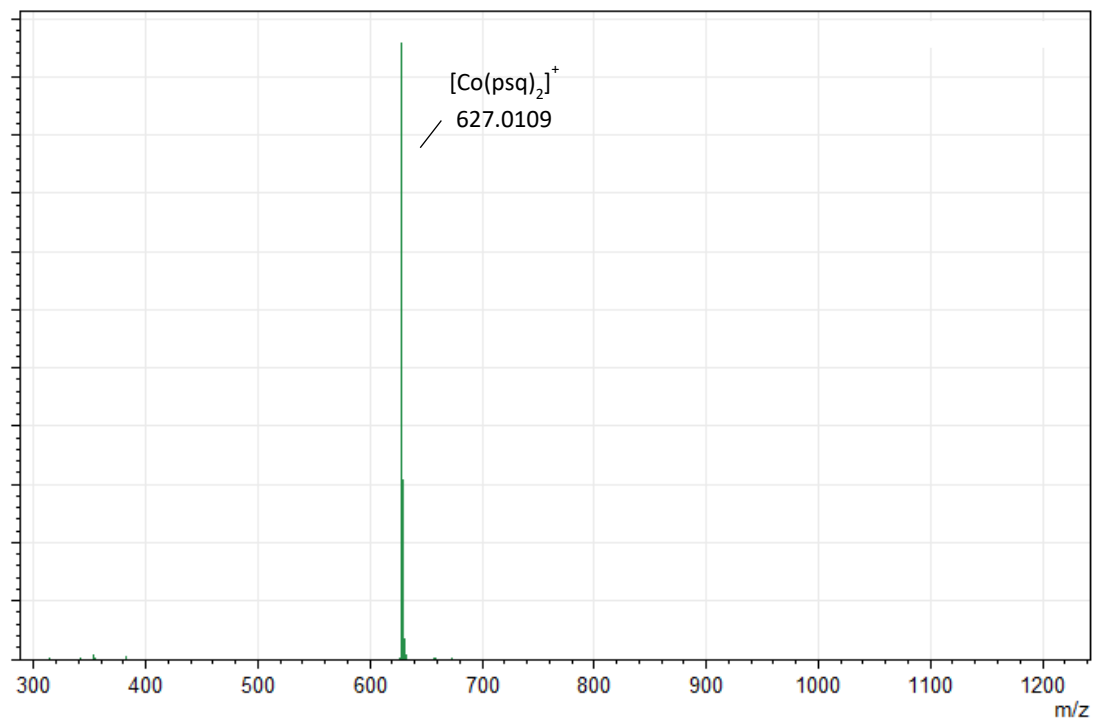


Figure S13. Mass spectrum (ESI, positive mode, MeCN) of $[\text{Co}(\text{psq})_2]\text{PF}_6$.

Zn(II)(psq)₂

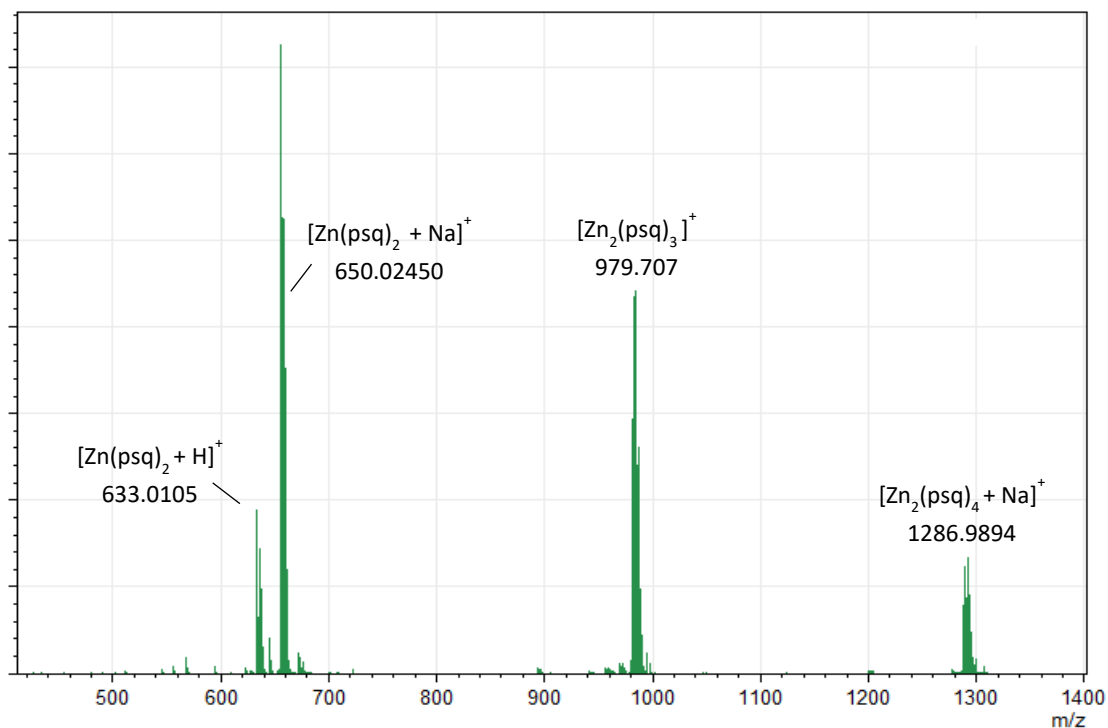


Figure S14. Mass spectrum (ESI, positive mode, MeCN) of Zn(psq)₂.

Electrochemical data

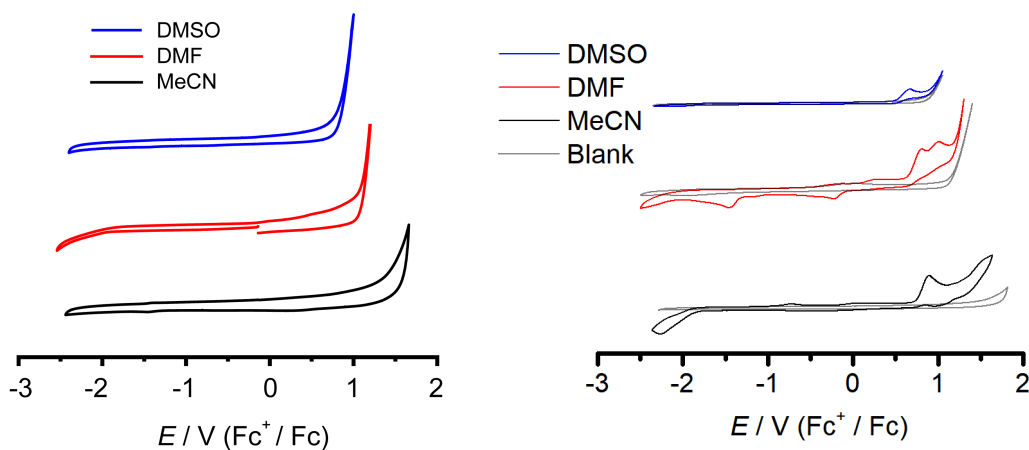


Figure S15. Left: Blank Cyclic Voltammograms of 0.1 M [Bu₄N]PF₆ in solvents as indicated Right: Cyclic voltammograms of 0.25 mM Hpsq in solvents as indicated (overlaid onto blank spectra in grey). Conditions: [Bu₄N]PF₆ (0.1 M), Glassy Carbon Working Electrode (1 mm), $\nu = 100 \text{ mV s}^{-1}$, ambient temperature.

Table S7. Electrochemical data extracted from figure 5. All potentials are given against Fc⁺/Fc.

	$E^{1/2} / \text{V}$ Co(II)/Co(I)	$E_{\text{sep}} / \text{V}$ Co(II)/Co(I)	I_a/I_c Co(II)/Co(I)	$E^{1/2} / \text{V}$ Co(III)/Co(II)	$E_{\text{sep}} / \text{V}$ Co(III)/Co(II)	I_a/I_c Co(II)/Co(I)	$\Delta E / \text{V}$	C / mM
DMF	-2.15	0.220	1.06	-0.380	0.220	1.07	1.77	115
DMSO	-1.95	0.082	1.03	-0.209	0.220	1.06	1.74	86
MeCN	-1.99	0.080	1.03	-0.265	0.094	1.03	1.75	12

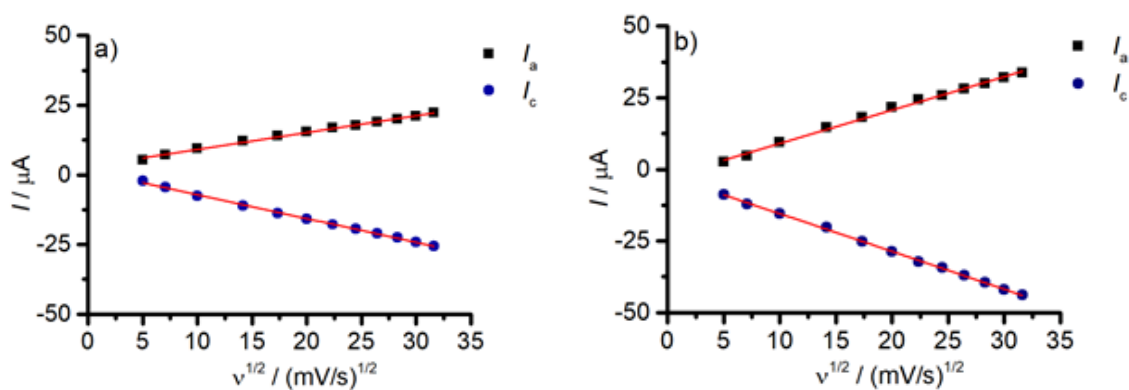


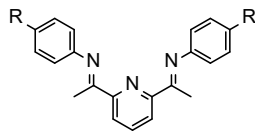
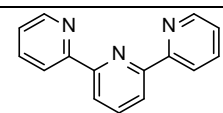
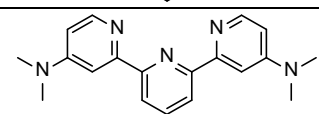
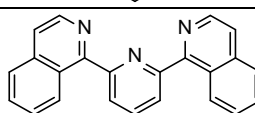
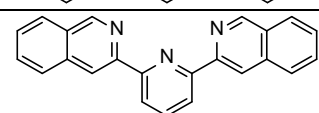
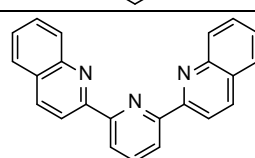
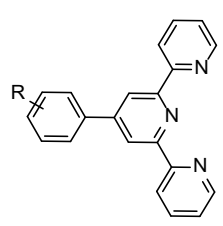
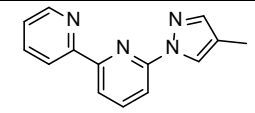
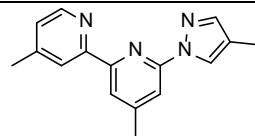
Figure S16. Current response (I) as a function of the square root of scan rate ($v^{1/2}$) for $\text{Co}(\text{psq})_2$ in MeCN (0.1 M $[\text{Bu}_4\text{N}]\text{PF}_6$) for the redox couples: a) $\text{Co}(\text{III})/\text{Co}(\text{II})$ and b) $\text{Co}(\text{II})/\text{Co}(\text{I})$. Calculated linear regressions are given as a red line.

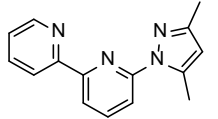
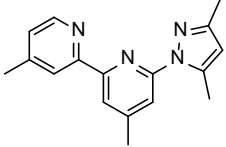
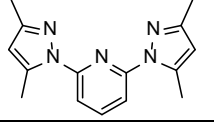
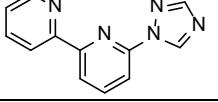
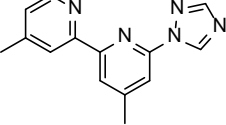
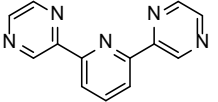
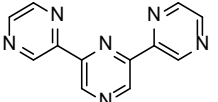
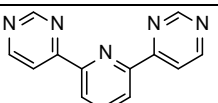
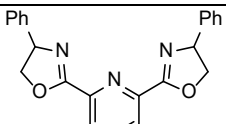
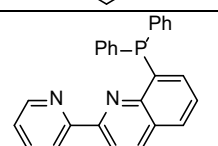
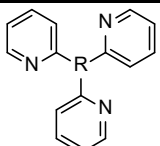
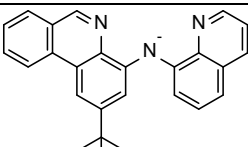
Table S8. Calculated linear regressions (equation) and approximations of diffusion constants (D_0) and hydrodynamic radii (\AA), based on the data shown in Figure S16.

	Fit	R^2	$ D_0 ^a$ $/ 10^{-9} \cdot \text{m}^2/\text{s}$	a^b $/ \text{\AA}$
(I_a) $\text{Co}(\text{II})/\text{Co}(\text{I})$	$I_{p,a} = 1.16 (v^{1/2}) - 2.55$	0.996	5.9	1.1
(I_c) $\text{Co}(\text{II})/\text{Co}(\text{I})$	$I_{p,c} = -1.32 (v^{1/2}) - 2.21$	0.999	7.6	0.85
(I_a) $\text{Co}(\text{III})/\text{Co}(\text{II})$	$I_{p,a} = 0.61 (v^{1/2}) - 3.10$	0.996	1.6	4.0
(I_c) $\text{Co}(\text{III})/\text{Co}(\text{II})$	$I_{p,c} = -0.86 (v^{1/2}) - 1.51$	0.998	3.2	2.0

^a estimated at 293.15K, ^b Stokes–Einstein radius.

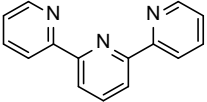
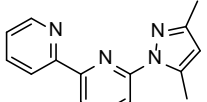
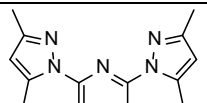
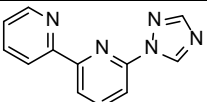
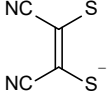
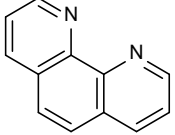
Table S9. Redox potentials for selected $[\text{Co}(\text{L}_2)]^{x+}$ complexes reported in the literature. The cyclic voltammograms are recorded in MeCN with a glassy carbon electrode. All potentials are given vs. Fc^+/Fc .

Ligand (L)	$E_{\text{ox}}^{1/2} / \text{V}$ Co(III)/Co(II)	$E_{\text{red}}^{1/2} / \text{V}$ Co(II)/Co(I)	$E_{\text{cell}} / \text{V}$ $ E_{\text{red}}^{1/2} - E_{\text{ox}}^{1/2} $	Electrolyte	Ref
Meridional Coordination					
 R: CN R: CF ₃ R: H R: Me R: OMe R: N(Me) ₂	0.39 0.35 0.11 0.03 -0.01 -0.20	-0.65 -0.70 -0.87 -0.92 -0.94 -1.05	1.04 1.05 0.98 0.95 0.93 0.85	TBABF ₄	1
	-0.09	-1.15	1.07	TBAPF ₆	2
	0.25 ^e	-1.52	1.77	$E_{\text{ox}}^{1/2} = \text{LiTFSI}$ $E_{\text{red}}^{1/2} = \text{TBAClO}_4$	3
	-0.09	-0.82	0.73	$E_{\text{ox}}^{1/2} = \text{LiTFSI}$ $E_{\text{red}}^{1/2} = \text{TBAClO}_4$	3
	-0.21	-1.32	1.11	$E_{\text{ox}}^{1/2} = \text{LiTFSI}$ $E_{\text{red}}^{1/2} = \text{TBAClO}_4$	3
	0.84 ^d	-0.89	1.73	$E_{\text{ox}}^{1/2} = \text{LiTFSI}$ $E_{\text{red}}^{1/2} = \text{TBAClO}_4$	3
 2-CF ₃ 2,6-F 2-OMe 2,4-OMe 2,4,6-OMe 4-OMe 3,4,5-OMe 3-OMe 3-CF ₃ , 4-OMe 3,5-OMe 3-Br 3-CF ₃ 4-CF ₃ 3,5-F 3,4,5-F 3,5-Br 3,5-CF ₃	-0.052 -0.063 -0.142 -0.171 -0.156 -0.162 -0.147 -0.136 -0.138 -0.137 -0.119 -0.115 -0.104 -0.095 -0.091 -0.096 -0.084	-1.094 -1.079 -1.175 -1.198 -1.212 -1.194 -1.153 -1.146 -1.149 -1.145 -1.118 -1.111 -1.094 -1.082 -1.076 -1.076 -1.055	1.042 1.016 1.033 1.027 1.056 1.032 1.006 1.01 1.011 1.008 0.999 0.996 0.99 0.987 0.985 0.98 0.971	TBABF ₄	4
	0.17	-1.24	1.41	TBAPF ₆	5
	0.11	-1.34	1.45	TBAPF ₆	5

	0.160	-1.22	1.37	TBAPF ₆	2	
	0.05	-1.37	1.42	TBAPF ₆	5	
	0.54 ^d	-1.37	1.91	TBAPF ₆	2	
	0.43	-1.08	1.51	TBAPF ₆	2	
	0.39	-1.19	1.58	TBAPF ₆	5	
	0.12	-0.81	0.93	TBAPF ₆	6	
	0.49	-0.49	0.98	TBAPF ₆	6	
	0.25	-0.86	1.11	TBAPF ₆	6	
	0.72	-0.83	1.55	TBAPF ₆	7a	
	-0.46	-1.06	0.60	TBAPF ₆	8	
Average Value	0.121	-1.03	1.21	-	-	
Facial Coordination						
	R: COH	-0.19	-1.55	1.36	TBAPF ₆	9a,e
	R: P	0.17	-1.36	1.52		
	R: Me	-0.16	-1.60	1.43		
	R: PO	0.61	-1.14	1.74		
	R: N	-0.73	-1.50	0.76		
		-1.30	-2.23 ^b	0.93	TBAPF ₆	10c
Average Value		-0.267	-1.43	1.29	-	-

^aSee ref: ¹¹ for conversion to Fc⁺/Fc, ^bnot explicitly characterized as Co(II)/Co(I), ^cisolated as a Co³⁺, ^dslow kinetics under given conditions, ^emeasured at a Pt-electrode.

Table S10. Theoretical energy density and max concentration measured in MeCN for selected $[\text{Co}(\text{L}_x)]^{x+}$ complexes reported in the literature.

Ligand (L)	Concentration / M	$\hat{E} / \text{Wh L}^{-1}$	Ref.
	0.18	2.58	2
	0.22	4.03	2
	0.50	12.80	2
	0.16	3.24	2
	0.39	8.8	12
	0.41	8.0	13

Charge-Discharge Cycling Experiments

The ohmic resistance of the cell was measured with electrochemical impedance spectroscopy in the frequency range 1 Hz – 200 kHz and was observed to be approximately 150 Ω . This yields an ohmic drop of 75 mV with an applied current of 500 mA and with 250 mA it yields an ohmic drop of 37.5 mV. The observed cell overpotential with a current of 500 mA is estimated to be 100 mV based on charge-discharge data $((E_{\text{avg, ch}} - E_{\text{avg, disch}}) / 2)$. Thus, 75% of the cell overpotential is due to the ohmic drop while the remaining 25% can be attributed to mass transfer and kinetic polarization resistances. The current density is given based on the surface of the membrane (Daramic HD polyethylene). A glass H-cell (Adams & Chittenden) with 5 mL compartments was used for charge-discharge experiments. The area of the membrane used to separate the two sides in the H-cell was 0.67 cm^2 , corresponding to a current density of 0.36 mA/cm^2 (250 mA) for the first cycle and 0.74 mA/cm^2 (500 mA) for the subsequent cycles. The carbon cloth is Plain Carbon Cloth 1071 HCB manufactured by AvCarb Material Solutions.

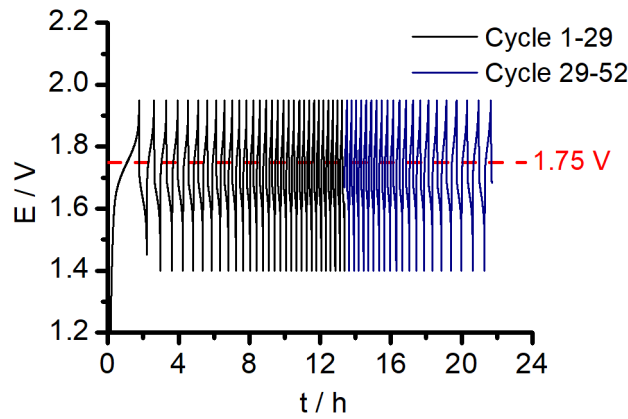


Figure S17. 52 charge-discharge cycles of 4.68 mM of $\text{Co}(\text{psq})_2$ in MeCN (1 M $(\text{NEt}_4)\text{PF}_6$) at $\pm 498 \mu\text{A}$, 1.4 V and 1.95 V is used as the lower and upper thresholds, the first 29 cycles is in black and the last 23 in blue, red dashed line indicate the theoretical cell potential.

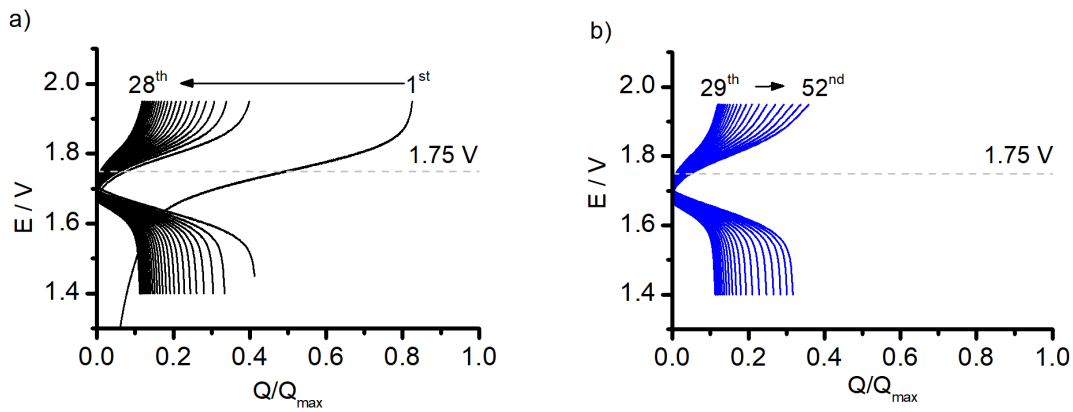


Figure S18. Cell potentials vs. capacity for the galvanostatic cycling of 4.65 mM $\text{Co}(\text{psq})_2$ in MeCN (1 M NEt_4PF_6) with a constant current ($498 \mu\text{A}$) for a) the first 28 cycles (black) and b) 29-52 cycles (blue). The grey line indicates the theoretical cell potential.

The energy efficiency (EE), coulombic efficiency (CE), relative discharge/charge capacity, maximum capacity and capacity fade rate are calculated from equation 1, 2, 3 and 4.¹⁴

$$\text{EE}\% = \frac{I_{\text{discharge}} \int_{t_{\text{start}}}^{t_{\text{end}}} E_{\text{discharge}} dt}{I_{\text{charge}} \cdot \int_{t_{\text{start}}}^{t_{\text{end}}} E_{\text{charge}} dt} \cdot 100 \quad (1)$$

$$\text{CE}\% = \frac{Q_{\text{discharge}}}{Q_{\text{charge}}} \cdot 100 \quad (2)$$

$$\text{Discharge/charge capacity} = \frac{Q_{\text{cycle } x}}{Q_{\text{theoretical}}} \cdot 100 \quad (3)$$

$$\text{Capacity fade rate} = \frac{(Q_{\text{cycle } 1} - Q_{\text{cycle } x}) \cdot Q_{\text{cycle } x}}{Q_{\text{theoretical}} \cdot n_{\text{cycles}}} \quad (4)$$

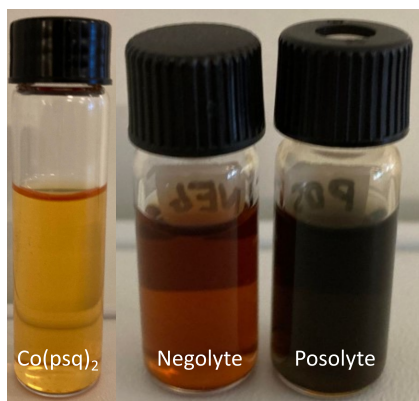


Figure S19. Picture of $\text{Co}(\text{psq})_2$ (left) before charge/discharge cycling the negolyte (middle), posolyte (right) after galvanostatic charge/discharge cycling.

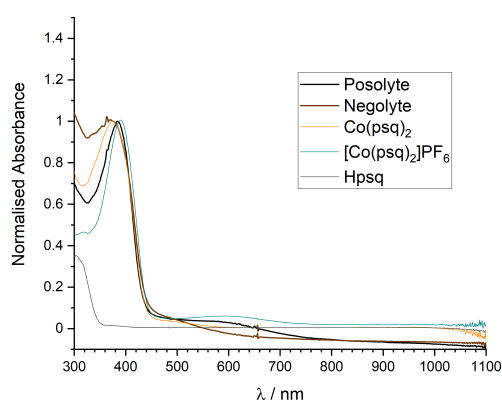


Figure S20. UV-vis absorption spectra of the posolyte solution (black) and the negolyte solution (dark brown) diluted in acetonitrile, overlaid onto the normalised spectra of $\text{Co}(\text{psq})_2$ (orange), $[\text{Co}(\text{psq})_2]\text{PF}_6$ (dark cyan) and Hpsq (grey) from Figure 2.

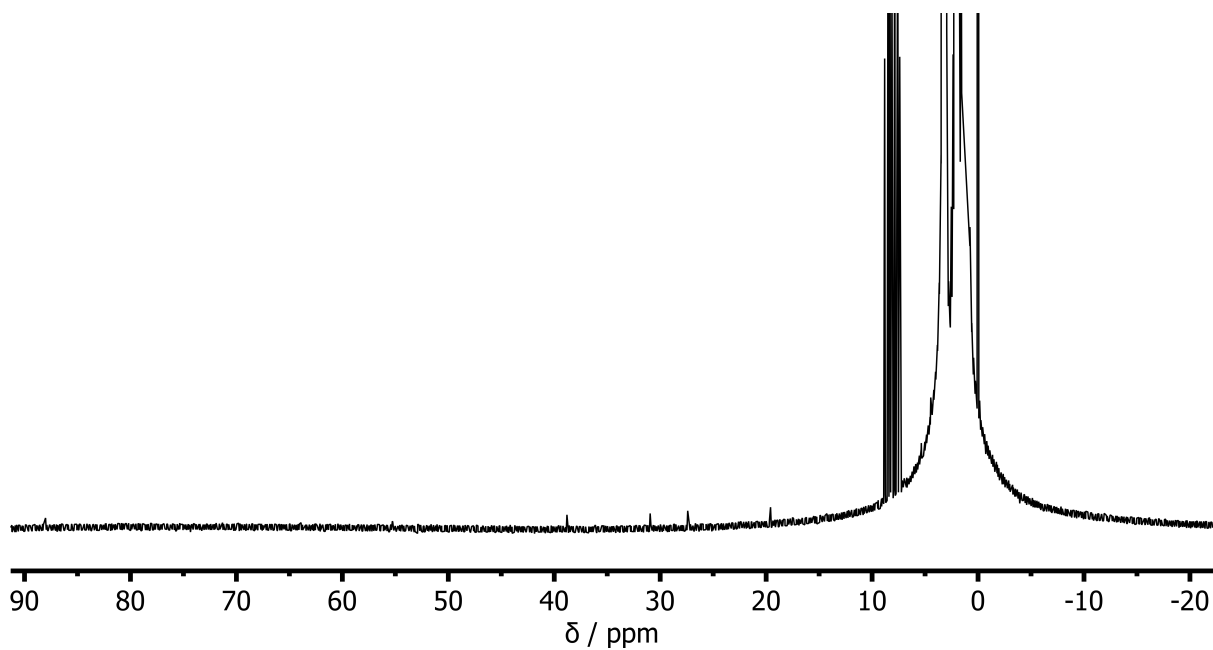


Figure S21. ^1H -NMR spectrum (400 MHz, CD_3CN) from 95 ppm to -20 ppm of the posolyte solution after galvanostatic charge/discharge experiments.

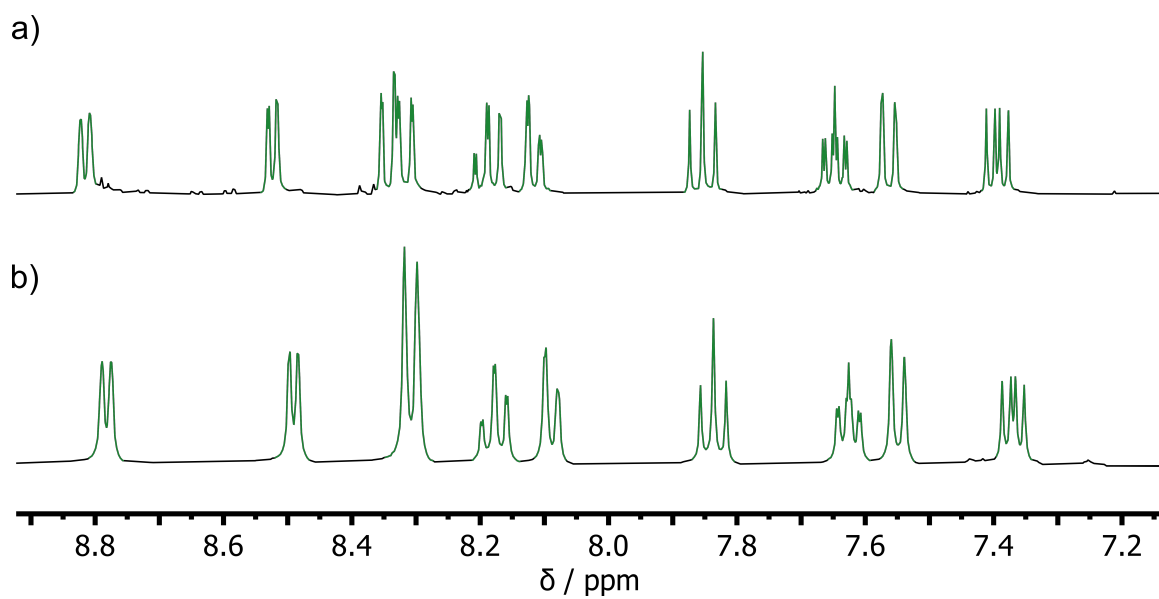


Figure S22. Stacked ^1H -NMR spectrum (400 MHz, CD_3CN) from 8.8 ppm to 7.2 ppm of $[\text{Co}(\text{psq})_2]\text{PF}_6$ and b) the posolyte solution after galvanostatic charge/discharge experiments. The green-colored signals are assigned as $[\text{Co}(\text{psq})_2]\text{PF}_6$.

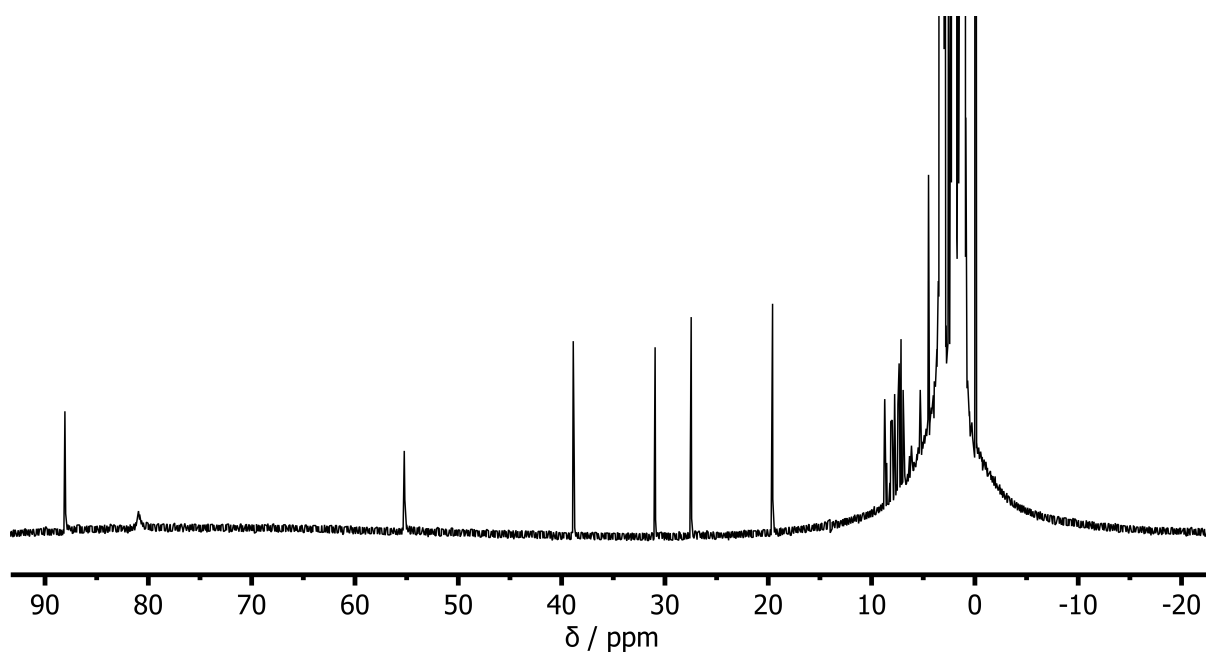


Figure S23. ^1H -NMR spectrum (400 MHz, CD_3CN) from 95 ppm to -20 ppm of the negolyte solution after galvanostatic charge/discharge experiments.

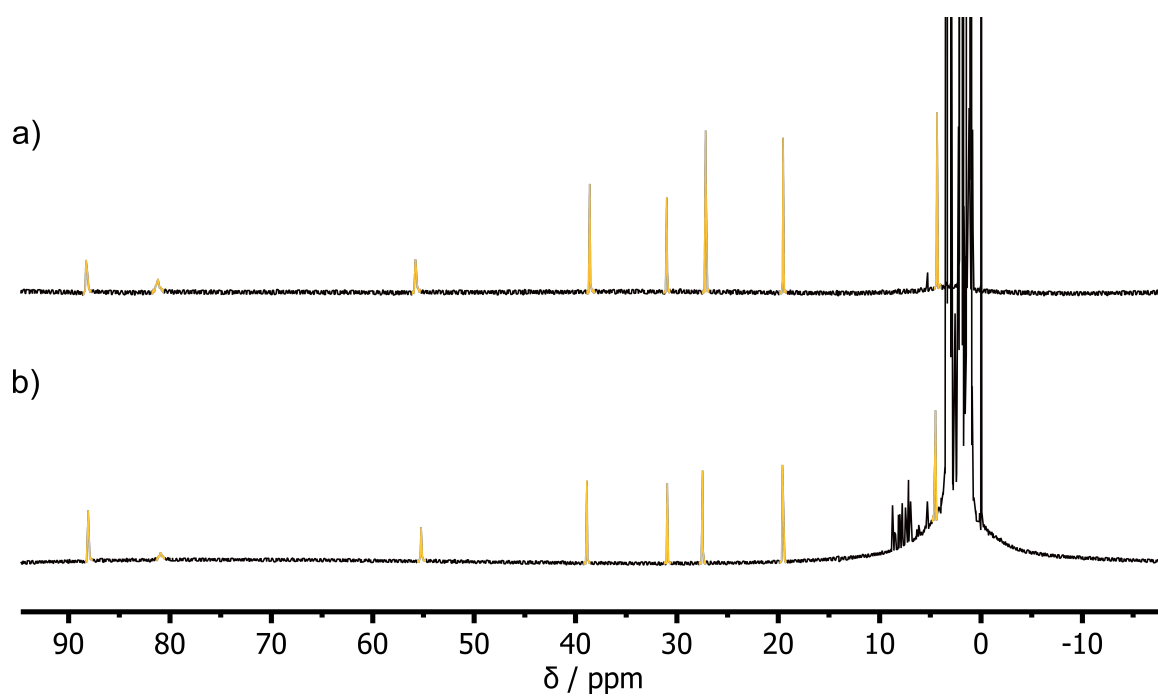


Figure S24. Stacked ^1H -NMR spectrum (400 MHz, CD_3CN) from 95 ppm to -10 ppm of a) $\text{Co}(\text{psq})_2$ and b) the negolyte solution after galvanostatic charge/discharge experiments. The orange-colored signals are assigned as $\text{Co}(\text{psq})_2$.

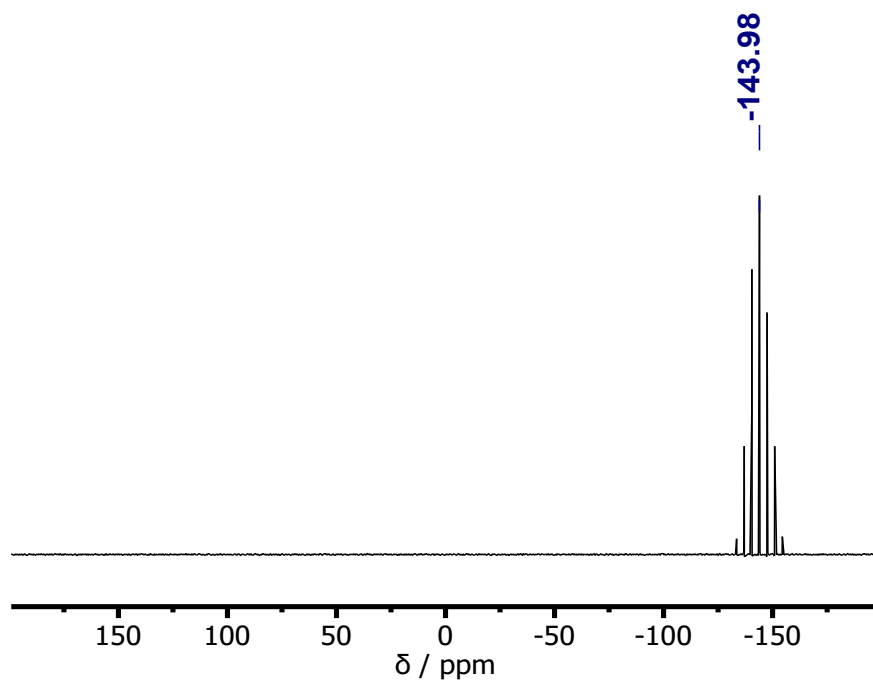


Figure S25. ^{31}P -NMR spectrum of (202 MHz, CD_3CN) from 160 ppm to -160 ppm of the electrolyte solution after galvanostatic charge/discharge experiments.

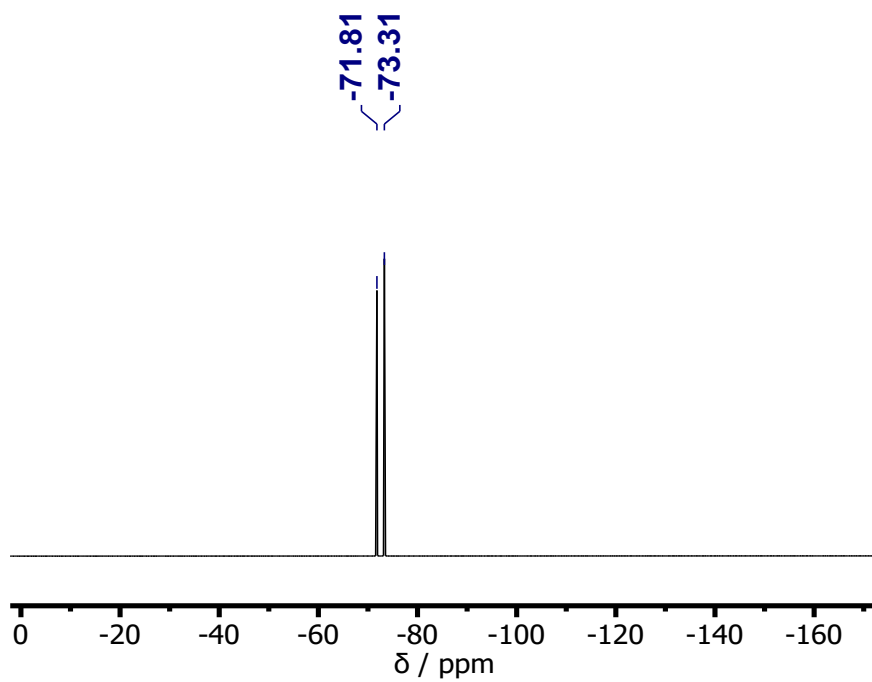


Figure S26. ^{19}F -NMR spectrum of (471 MHz, CD_3CN) from 160 ppm to -160 ppm of the electrolyte solution after galvanostatic charge/discharge experiments.

Electron Accounting

The following scenarios were considered and modelled in an attempt to reconcile the number of electrons consumed against the amount of 8-aminoquinoline that was produced (Scheme S1 and Figure S27).

Scenario One

The first scenario we considered was that following reduction of $[\text{Co}^{\text{II}}(\text{psq})_2]$, dissociation of one psq^- ligand would form new species, most likely supported by acetonitrile, though we introduced a general term 'L' to describe any ligating group. Reduction of the dissociated psq^- would consume a second electron, and generate 8-AQ.

1a: The new $[\text{Co}^{\text{I}}(\text{psq})(\text{L})_x]$ species is redox inert (top scheme in the blue zone Figure S27)

If this $[\text{Co}^{\text{I}}(\text{psq})(\text{L})_x]$ species was redox inactive (within the cycling potentials), then, indeed, this electron would be 'wasted' and 'lost'.

Net change per 8-AQ: 2 equivalents of electrons and 1 equivalent of $[\text{Co}(\text{psq})_2]$ decomposition.

1b: The new $[\text{Co}^{\text{I}}(\text{psq})(\text{L})_x]$ species is redox active (left hand side reactions in the bottom zone of Figure S27)

If these complexes remain redox active, within the operating window of the device, then the electrons stored in the $[\text{Co}^{\text{I}}(\text{psq})(\text{L})_x]$ species would still be available during the discharge (albeit at lower energy), hence 'refunded' (left hand side reactions in the dark purple region of Figure S27).

Net change per 8-AQ: 1 equivalent of electrons and 1 equivalent of $[\text{Co}(\text{psq})_2]$ decomposition. (No change in number of redox active cobalt centres).

1c: Two $[\text{Co}^{\text{I}}(\text{psq})(\text{L})_x]$ species disproportionate to $[\text{Co}^{\text{II}}(\text{psq})_2]$ and a Co^0L_y (bottom scheme in the blue zone of Figure S27).

A total of four electrons are consumed (2 per cobalt), and 2 equivalents of 8-AQ are produced. One equivalent of $\text{Co}(\text{psq})_2$ is recovered.

Net change per 8-AQ: 2 equivalents of electrons but only half an equivalent of $[\text{Co}(\text{psq})_2]$ decomposition.

Scenario Two

The second scenario we considered was that following reduction of $[\text{Co}^{\text{II}}(\text{psq})_2]$, dissociation of **both** psq^- ligands would form new species, most likely supported by acetonitrile as the reviewer has suggested below, we left it with a 'naked,' generic formulation: "Co^I". Reduction of the dissociated psq^- would consume two more electrons, and generate two equivalents of 8-AQ.

2a: The new $[\text{Co}^{\text{I}}]$ species is redox inert (middle region Figure S27)

If this $[\text{Co}^{\text{I}}]$ species was redox inactive (within the cycling potentials), then, indeed, this electron would be 'wasted' and 'lost'. Net change per 8-AQ: 1.5 equivalents of electrons and 1 equivalent of $[\text{Co}(\text{psq})_2]$ decomposition.

2b: The new $[\text{Co}^{\text{I}}]$ species is redox active (right hand side reactions in the bottom zone of Figure S25)

If these complexes remain redox active, within the operating window of the device, then the electron stored in the $[\text{Co}^{\text{I}}]$ species would still be available during the discharge (albeit at lower energy), hence 'refunded' (left hand side reactions in the dark purple region of Figure S27).

Net change per 8-AQ: 1 equivalents of electrons and 0.5 equivalents of $[\text{Co}(\text{psq})_2]$ decomposition. (No change in number of redox active cobalt centres).

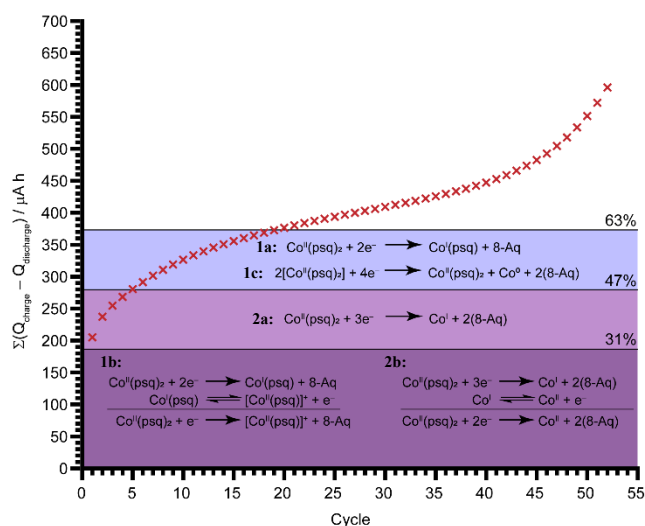
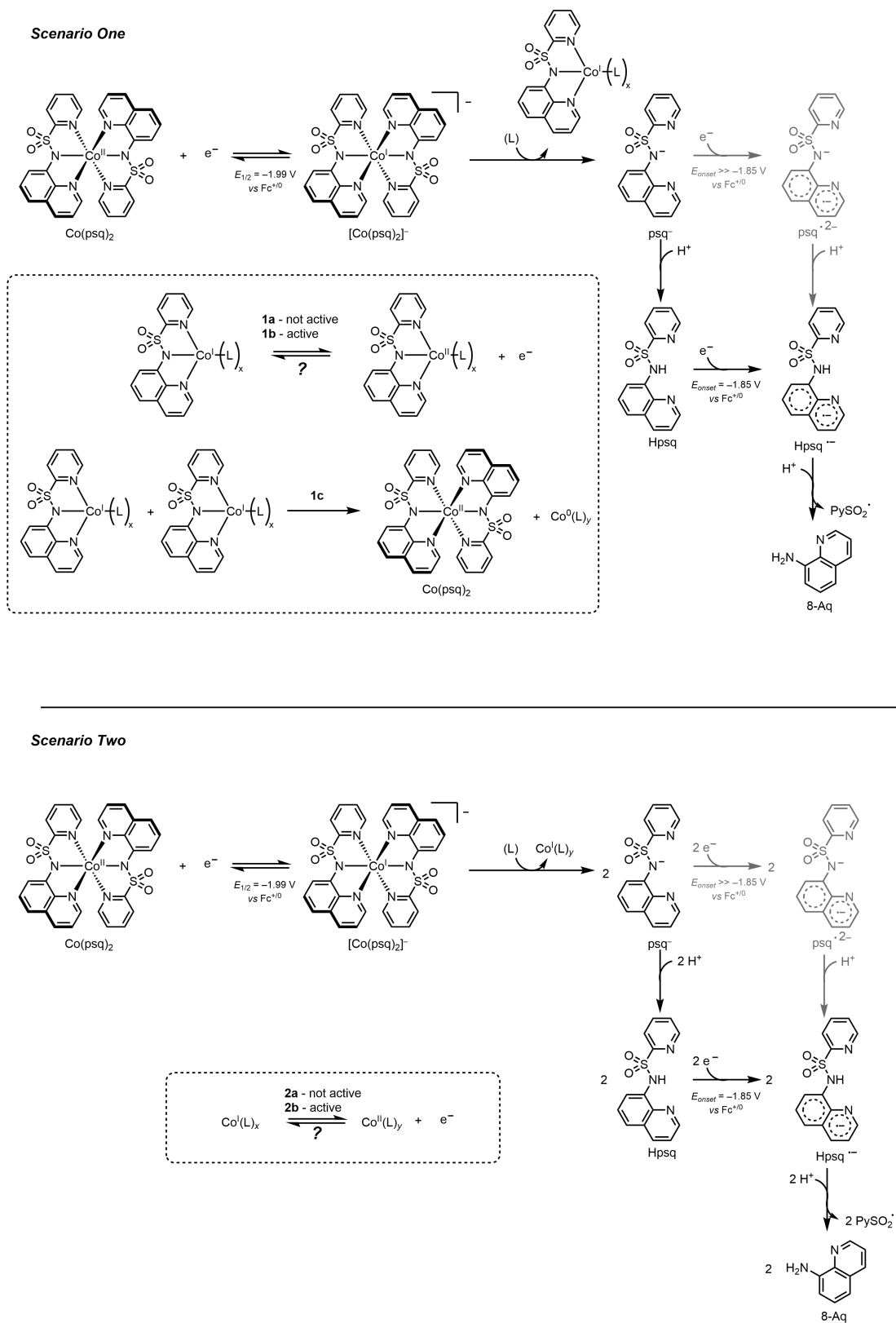


Figure S27. The cumulative charge lost over the course of 52 galvanostatic charge-discharge cycles (red crosses) compared to the amount of charge required to generate the 1.74 mM 8-aminoquinoline (8-Aq) found in the negolyte at the conclusion depending on the different possible reaction pathways (shaded regions).



Scheme S1. Two plausible pathways for the reductive cleavage of Hpsq to 8-aminoquinoline (8-Aq) via proton-coupled electron transfer following reduction of $\text{Co}^{\text{II}}(\text{psq})_2$ and dissociation of psq^- . Inset are shown exemplar redox or disproportionation reactions for the Co^{I} species formed following dissociation of one or both psq ligands. In the scheme, “L” represents any combination of co-ligands (e.g., MeCN solvent and/or 8-aminoquinoline) which may interact with the cobalt centres.

References

- (1) Araujo, C. M.; Doherty, M. D.; Konezny, S. J.; Luca, O. R.; Usyatinsky, A.; Grade, H.; Lobkovsky, E.; Soloveichik, G. L.; Crabtree, R. H.; Batista, V. S. Tuning redox potentials of bis(imino)pyridine cobalt complexes: an experimental and theoretical study involving solvent and ligand effects. *Dalton Trans.* **2012**, 41 (12), 3562–3573.
- (2) Armstrong, C. G.; Toghill, K. E. Cobalt(II) complexes with azole-pyridine type ligands for non-aqueous redox-flow batteries: Tunable electrochemistry via structural modification. *J. Power Sources* **2017**, 349, 121–129.
- (3) Aroua, S.; Todorova, T. K.; Hommes, P.; Chamoreau, L.-M.; Reissig, H.-U.; Mougel, V.; Fontecave, M. Synthesis, Characterization, and DFT Analysis of Bis-Terpyridyl-Based Molecular Cobalt Complexes. *Inorg. Chem.* **2017**, 56 (10), 5930–5940.
- (4) Dickenson, J. C.; Haley, M. E.; Hyde, J. T.; Reid, Z. M.; Tarring, T. J.; Iovan, D. A.; Harrison, D. P. Fine-Tuning Metal and Ligand-Centered Redox Potentials of Homoleptic Bis-Terpyridine Complexes with 4'-Aryl Substituents. *Inorg. Chem.* **2021**, 60 (13), 9956–9969.
- (5) Shavaleev, N. M.; Kessler, F.; Grätzel, M.; Nazeeruddin, M. K. Redox properties of cobalt(II) complexes with azole-pyridines. *Inorg. Chim. Acta* **2013**, 407, 261–268.
- (6) Cook, L. J. K.; Tuna, F.; Halcrow, M. A. Iron(II) and cobalt(II) complexes of tris-azanyl analogues of 2,2':6',2'-terpyridine. *Dalton Trans.* **2013**, 42 (6), 2254–2265.
- (7) Cabort, A.; Michel, A.; Therrien, B.; Stoeckli-Evans, H.; Bernauer, K.; Süß-Fink, G.; Williams, A. F.; Stupka, G. Iron, cobalt, nickel and ruthenium complexes of 2,6-bis(3,4-dihydro-2H-pyrrol-5-yl)pyridine, a pybox analogue. *Inorg. Chim. Acta* **2003**, 350, 193–200.
- (8) Talukdar, K.; Issa, A.; Jurss, J. W. Synthesis of a Redox-Active NNP-Type Pincer Ligand and Its Application to Electrocatalytic CO₂ Reduction With First-Row Transition Metal Complexes. *Front. Chem.* **2019**, 7, 330.
- (9) Adam, K. R.; Anderson, P. A.; Astley, T.; Atkinson, I. M.; Charnock, J. M.; Garner, C. D.; Gulbis, J. M.; Hambley, T. W.; Hitchman, M. A.; Keene, F. R.; et al. Stabilization of cobalt(I) by the tripodal ligands tris(2-pyridyl)methane and tris(2-pyridyl)phosphine. Structural, spectroscopic and ab initio studies of the [CoL₂]ⁿ⁺ species. *J. Chem. Soc., Dalton Trans.* **1997**, No. 4, 519–530.
- (10) Braun, J. D.; Lozada, I. B.; Herbert, D. E. In Pursuit of Panchromatic Absorption in Metal Coordination Complexes: Experimental Delineation of the HOMO Inversion Model Using Pseudo-Octahedral Complexes of Diarylamido Ligands. *Inorg. Chem.* **2020**, 59 (23), 17746–17757.
- (11) Pavlishchuk, V. V.; Addison, A. W. Conversion constants for redox potentials measured versus different reference electrodes in acetonitrile solutions at 25°C. *Inorg. Chim. Acta* **2000**, 298 (1), 97–102.
- (12) Hogue, R. W.; Armstrong, C. G.; Toghill, K. E. Dithiolene Complexes of First-Row Transition Metals for Symmetric Nonaqueous Redox Flow Batteries. *ChemSusChem* **2019**, 12 (19), 4506–4515.
- (13) Xing, X.; Zhang, D.; Li, Y. A non-aqueous all-cobalt redox flow battery using 1,10-phenanthrolinecobalt(II) hexafluorophosphate as active species. *J. Power Sources* **2015**, 279, 205–209.
- (14) Yao, Y.; Lei, J.; Shi, Y.; Ai, F.; Lu, Y.-C. Assessment methods and performance metrics for redox flow batteries. *Nat. Energy* **2021**.